RESEARCH ARTICLE | MAY 29 2024

Comprehending flame development and misfire at advanced engine conditions: Detailed experimental characterizations and machine learning-assisted kinetic analyses

Yanqing Cui (崔雁清) ; Haifeng Liu (刘海峰) ; Mingsheng Wen (文铭升) ; Zhenyang Ming (明镇洋); Zunqing Zheng (郑尊清) ; Yu Han (韩禹) ; Song Cheng (成松) ; Mingfa Yao (尧命发)

Physics of Fluids 36, 055161 (2024)
https://doi.org/10.1063/5.0211783

Physics of Fluids ARTICLE pubs.aip.org/aip/pof

Comprehending flame development and misfire at advanced engine conditions: Detailed experimental characterizations and machine learning-assisted kinetic analyses

Cite as: Phys. Fluids **36**, 055161 (2024); doi: 10.1063/5.0211783
Submitted: 2 April 2024 · Accepted: 10 May 2024 ·
Published Online: 29 May 2024

Yanqing Cui (崔雁清),[1,2,3] Haifeng Liu (刘海峰),[1,a)] Mingsheng Wen (文铭升),[1] Zhenyang Ming (明镇洋),[1] Zunqing Zheng (郑尊清),[1] Yu Han (韩禹),[2] Song Cheng (成松),[2,a)] and Mingfa Yao (尧命发)[1]

AFFILIATIONS

[1]State Key Laboratory of Engines, Tianjin University, Tianjin 300072, China
[2]Department of Mechanical Engineering, The Hong Kong Polytechnic University, Hong Kong, China
[3]Department of Industrial and Systems Engineering, The Hong Kong Polytechnic University, Hong Kong, China

[a)]**Authors to whom correspondence should be addressed:** haifengliu@tju.edu.cn and songryan.cheng@polyu.edu.hk

ABSTRACT

Through comprehensive experimental and modeling efforts, this work unravels the underlying mechanisms governing flame development and misfire at advanced engine conditions that are representative of low-load and lean blow-out operations. Toward this, preliminary heat release, autoignition, and flame developing patterns are characterized, via a case study of n-heptane, at ultra-lean conditions in a well-controlled optical engine under various combustion modes including homogeneous charge compression ignition (HCCI), partially premixed combustion (PPC), and reactivity-controlled compression ignition (RCCI). Changes in preliminary heat release and flame developing patterns at three overall equivalence ratios (0.12, 0.18, and 0.24) are first characterized under the PPC mode. Flame development characteristics including flame areas and number of initial flame kernels at close-to-misfire conditions are further extracted and compared across the HCCI, RCCI, and three PPC modes, with two distinctive and one transition regimes identified. Further analyses indicate that sustainable flame development and misfire are largely controlled by the spatial distribution of local equivalence ratio (phi) and local temperature in the mixture, which dictate the initial flame kernel generation and the subsequent flame propagation through localized preliminary heat release and autoignition. Chemical kinetic modeling is also undertaken, using a recently updated gasoline chemistry model, in conjunction with a backpropagation neural network, where the predicted ignition delay map well captures the different regions of flame development. Further kinetic analysis and heat rate of production per reaction analysis corroborate the CH_2O planar laser-induced fluorescence experiments and highlight the important chemical kinetics that govern the initial flame development patterns.

NOMENCLATURE

AI	Artificial intelligence
BP	Backpropagation
CEMA	Chemical explosive mode analysis
CNN	Convolutional neural network
DNS	Direct numerical simulation
FWHM	Full width at half maxima
HCCI	Homogeneous charge compression ignition
HRR	Heat release rate
HTHR	High temperature heat release
ICE	Internal combustion engine
LLNL	Lawrence Livermore National Laboratory
LPM	Lean-premixed
LTR	Low temperature reactions
LTHR	Low temperature heat release
MRE	Mean relative error
MSE	Mean square error
NTC	Negative temperature coefficient
Phi	Equivalence ratio
PLIF	Planar laser-induced fluorescence
PPC	Partially premixed combustion
RCCI	Reactivity-controlled compression ignition
UHC	Unburnt hydrocarbon

I. INTRODUCTION

Partially premixed combustion (PPC) mode involves air–fuel mixture that exhibits partial mixing, falling between a fully homogeneous mixture and a non-premixed mixture. PPC is commonly utilized in reciprocating internal combustion engine (ICE) and gas turbine engines.[1–3] Benefiting from low engine-out emissions and better combustion controllability, PPC has aroused wide attention. Nevertheless, there are also some limitations for PPC. For instance, the lean-premixed (LPM) combustion mode in gas turbine combustor is often operated near the blow-out limit. The flow instability can cause equivalence ratio (phi) oscillation, which might further incur thermo-acoustic oscillation and combustion instabilities that damage the combustor.[1,4–7] In reciprocating ICE, the combustion instability can lead to decreased thermal efficiency, increased unburnt hydrocarbon (UHC) emissions, and enhanced cycle-to-cycle variations at low-load conditions.[2,8,9] Although the combustion devices are different, the combustion instability or the lean blow-out limit is a general issue that needs to be concerned at engine low-load conditions.

Combustion instability, or the lean blow-out limit, under engine low-load conditions is affected greatly by unsustainable flame development leading to misfire. Spray flame misfire mechanism has been investigated previously, both numerically and experimentally.[10–12] Liu *et al.*[10] numerically investigated the critical environment temperature for n-dodecane spray flame autoignition characteristics at low-load and cold-start conditions. Results showed that the low temperature reaction (LTR) area moves toward the downstream fuel spray as the ambient temperature decreases, resulting in insufficient heat release. The decomposition of H_2O_2 could not be triggered and misfire occurred. Shi *et al.*[11] numerically studied the influences of injection pressure on the autoignition behavior of n-dodecane spray flame. They found that with the injection pressure increasing, the total ignition delay decreased first and then increased due to the competition between the diffusion dominated first stage ignition delay and chemistry dominated second-stage induction time. The results were consistent with the experimental study from Chen *et al.*,[12] in which the ignition delay first shortened and then prolonged with the injection pressure increasing at quasi-critical ignition temperature. These studies involving flame misfire have mainly been focusing on spray flame using mostly numerical simulations, while there is an obvious lack of experimental investigations on misfire, let alone those involved in PPC. In addition, the underlying reason for misfire has barely been analyzed.

Identifying flame development pattern has been an effective method to determine whether misfire might occur. Multipoint autoignition pattern and flame propagation pattern are two typical flame development patterns found in reciprocating ICE. The criterion to determine either autoignition or flame propagation was proposed mainly via direct numerical simulation (DNS). Bansal *et al.*[13] proposed the Damköhler number of HO_2 species (Da_{HO2}) to determine the diffusion or reaction dominated combustion. They demarcated the ignition mode as quenching premixed flame when Da_{HO2} is less than 0.4, deflagration front when Da_{HO2} is between 0.4 and 1.4, spontaneous ignition front when Da_{HO2} is larger than 1.4. Many researchers, such as Yoo *et al.*,[14] Luong *et al.*,[15,16] Su *et al.*,[17] have also proposed criteria based on the Damköhler number to determine the flame development pattern. The determination method also includes chemical explosive mode analysis (CEMA),[18–20] ratio of different chemical reaction rates,[21] etc. Though the criterion to determine the autoignition or flame propagation has been proposed, it is mainly through numerical simulations, whereas experimental studies of the flame development pattern of PPC at or close to misfire conditions are scarce.

With recent advances in artificial intelligence (AI) technology, it has also been utilized to assist in monitoring the combustion instability. Zhou *et al.*[22] monitored combustion instability using a convolutional neural network (CNN) in the stratified swirl flame. Results showed that the CNN could effectively monitor the combustion state with an accuracy of 99%, and it showed a good generalization ability for eight unknown operation conditions. Wang *et al.*[23] designed a novel deep learning mode to detect the combustion condition in furnace and measured the heat release condition. The prediction mode achieved a predictive accuracy of 99.9% with the speed of 1 ms per image. Though the purely data-driven models have the ability to replicate experimental observations adequately, the poor generalization performance has made it challenging to extrapolate beyond uncharted conditions.[24] Overall, the AI-assisted combustion characterization has been widely utilized in various combustion devices, but it is mainly concentrated on the prediction of combustion state based on the time sequential images or videos without sufficient physical description.

To address these needs, this study targets to comprehend the underlying mechanisms governing misfire at a range of advanced engine conditions (HCCI, PPC, and RCCI) in a well-controlled optical engine. Toward this, heat release, autoignition, and flame development patterns are characterized via multiple optical diagnostic methods, including natural/OH^* flame natural luminosity imaging and fuel-tracer/formaldehyde planar laser-induced fluorescence (PLIF). Critical parameters that are representative of local mixture reactivity are extracted. The impact of these parameters on flame development patterns is analyzed through experimental observations, as well as kinetic analyses coupling a recently developed chemical kinetic model and a backpropagation (BP) neural network. Finally, the importance of individual reactions governing the preliminary heat release behavior is determined along with insights toward controlling flame development at advanced engine conditions.

II. METHODOLOGIES

A. Engine system

The experiments are conducted in a modified optical diesel engine. The schematic diagram of it is shown in Fig. 1. The detailed geometric parameters are summarized in our previous work.[25] The bore diameter and stroke are 92 and 100 mm, respectively. The compression ratio is set at approximately 11:1. The injector has six holes with the corresponding spray included angle of 150° and injector hole diameter of 0.15 mm. More details of the engine facility can be found in Ref. 25.

The schematic diagram of inside the cylinder is illustrated in Fig. 2. The combustion chamber shape is cylindrical. To allow the laser sheet entering, there is an incision with the width of 40 mm in the combustion chamber wall. During the experiments, the flame natural luminosity signal or the excited fluorescence signal passes through the quartz window, which is then reflected by the UV-enhanced reflection mirror and recorded by the horizontal-arranged camera.

B. Flame imaging technology

Multiple optical diagnostic methods are adopted in this study. Flame or OH^* natural luminosity imaging is performed without the

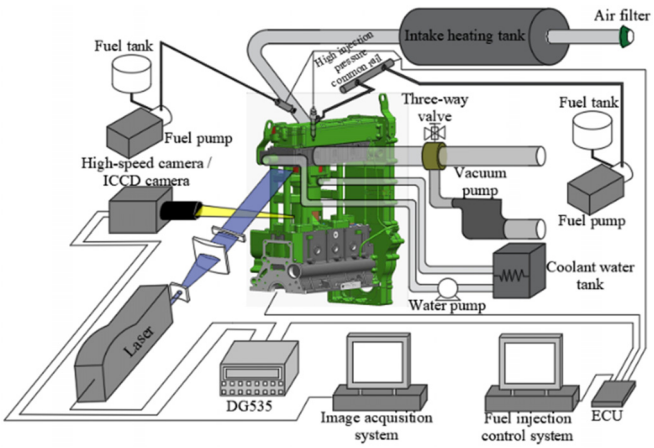

FIG. 1. The optical engine system.

utilization of laser, where the light signal is recorded through the high-speed camera or ICCD camera, respectively, in the experiment.

To record the flame natural luminosity images, a high-speed camera (Photron SA5) equipped with a focal length of 50 mm Nikon lens is used. The aperture number is set at F1.4. The shooting frequency is 20 000 frames per second (fps). The corresponding exposure time is 50 μs, which corresponds to a temporal resolution of 0.36 °CA when the engine speed is 1200 revolutions per minute (rpm).

To record the OH* natural luminosity images, an ICCD camera (DH734i-18F-03, Andor) equipped with a focal length of 100 mm ultraviolet Nikon lens is used. The wavelength of OH* chemiluminescence emission is between 306 and 310 nm.[26] To filter out the disturbance of other noise, two bandpass filters are mounted in front of the lens of the ICCD camera. One filter has a center wavelength of 320 nm with full width at half maxima (FWHM) of 40 nm. The other filter has a center wavelength of 315 nm with FWHM of 15 nm. The aperture of the lens is set at F4.5. The exposure time is 100 μs and gain level is 100. As for ICCD camera, limited by its shooting frequency, it can record only one image at each combustion event. Five images are averaged to eliminate the cycle-to-cycle variation.

C. Fuel-tracer/formaldehyde PLIF

The 266 nm laser (60 mJ/pulse) is utilized for fuel-tracer PLIF experiment, and the 355 nm laser (70 mJ/pulse), for formaldehyde PLIF experiment, respectively, which is generated from a Nd:YAG laser. The schematic diagram of the PLIF experiment is illustrated in Fig. 3. A laser sheet with 30 mm wide and 1 mm thick is formed through the cylindrical lens group, which is located in a plane 10 mm below the firedeck.

In the fuel-tracer PLIF experiments, acetone is utilized as the fuel tracer. The fluorescence spectrum of iso-octane (90%$_v$)/acetone (10%$_v$) mixture excited by the 266 nm laser with and without filter is illustrated in Fig. 4. Two Semrock filters, which include an edge filter and a long-pass filter, are utilized to isolate the 266 nm laser and to retain the light signal in the wavelength length of 390–475 nm. The ICCD camera was utilized with the exposure time of 50 ns and gain level of 200, respectively. The lens aperture is F4.5. The detailed imaging process can be found in previous work.[25] After the image post-processing, the in-cylinder local phi can be obtained. The local temperature can also be calculated by only considering the fuel evaporation effects.

In the formaldehyde PLIF experiment, a third harmonic laser of 355 nm is utilized. The spectrum of formaldehyde fluorescence is in the range 390–480 nm. The selection of filters group and the setup of ICCD camera are the same as those in the fuel-tracer PLIF experiment as mentioned earlier.

D. Engine operation conditions

The engine speed is 1200 rpm, and the skip-fire mode is utilized, with one combustion cycle in every other 20 continuous non-fired cycles. The purpose is to reduce the thermal stress and the failure on the visualization quartz window. The detailed parameters of engine operation conditions are summarized in Table I. The intake temperature is maintained at 125 °C. The coolant temperature is set at 95 °C to ensure stable engine operation. The DI fuel mass per cycle is adjusted at three levels, namely 4, 6, and 8 mg, which corresponds to an overall phi of 0.12, 0.18, and 0.24, respectively. The DI pressure and DI timing are also adjusted to create stable combustion or misfire condition.

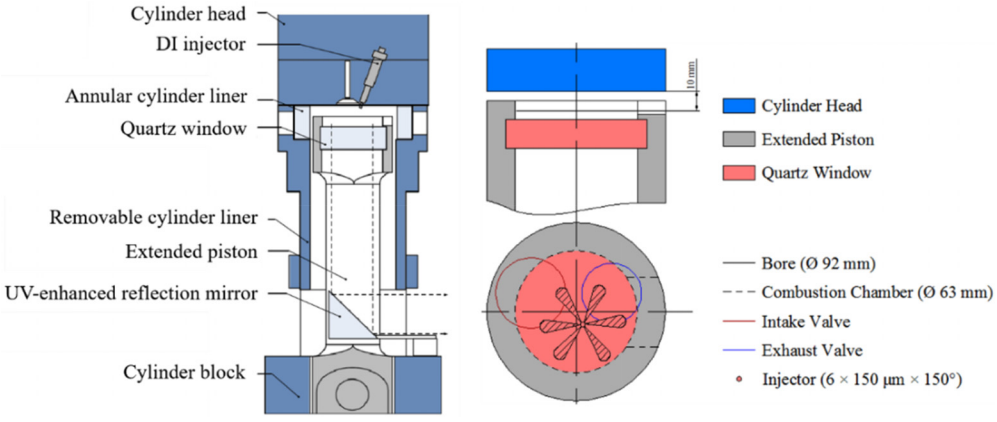

FIG. 2. Schematic diagram of the cylinder and combustion chamber.

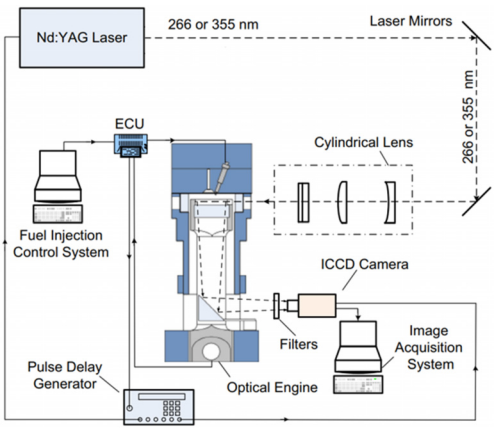

FIG. 3. Schematic diagram of the laser setup.

E. Chemical kinetic modeling and backpropagation (BP) neural network

The BP neural network structure is illustrated in Fig. 5. The parameters of phi and ambient temperature are selected as the input. The output parameter is the ignition delay. The dataset included 7216 groups of ignition delay points at conditions that are representative of the diesel engine, which are obtained through the closed homogeneous batch reactor in CHEMKIN PRO software. The chemical kinetic model developed by the Lawrence Livermore National Laboratory (LLNL) mechanism is selected to conduct the simulations.[27] In the simulations, the phi is between 0.25 and 2.0 with a step of 0.01. The mixture temperature is adjusted between 600 and 1000 K with a step of 10 K. The ambient pressure is fixed at 18 bar at 12 °CA based on the in-cylinder pressure curve, as justified below.

The testing set includes randomly selected 361 groups of the ignition delay points, which accounts for 5% of the total dataset. 90% of the total dataset are selected as the training set and 5% of the total dataset are selected as the validation set randomly.

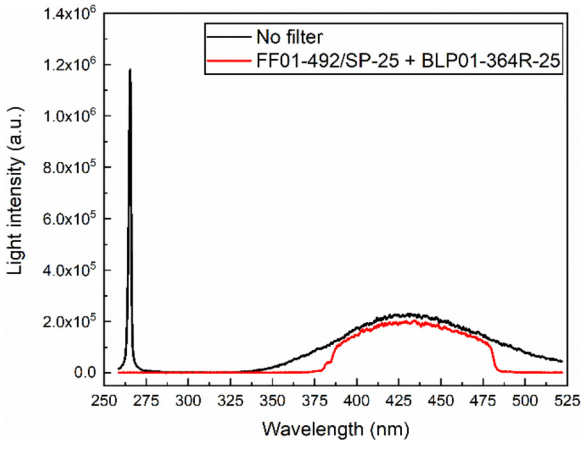

FIG. 4. Fluorescence spectrum of an iso-octane (90%$_v$)/acetone (10%$_v$) mixture excited by 266 nm laser with (red line) and without filter (black line).

TABLE I. Detailed parameters of engine operation conditions.

Parameter	Value
Engine speed/rpm	1200
Intake temperature/°C	125
Coolant temperature/°C	95
DI fuel	N-heptane
DI fuel mass per cycle/mg	4, 6, 8
Overall phi	0.12, 0.18, 0.24
DI pressure/bar	300, 600, 1000
DI timing/°CA ATDC	−25, −5

After optimizing the hyperparameters in the BP neural network, one hidden layer is obtained, and the number of neurons in the hidden layer is set at 15. The activation functions of *logsig* and *purelin* are utilized in the hidden layer and the output layer, respectively. The detailed mathematic expressions of them are shown in the following equations:

$$logsig: \sigma(z) = \frac{2}{1+e^{-z}}, \tag{1}$$

$$purelin: \sigma(z) = z. \tag{2}$$

Three metrics of Pearson correlation coefficient (R value), mean square error (MSE), and mean relative error (MRE) are utilized to evaluate its prediction performance. The detailed mathematic expressions of them are shown in Eqs. (3), (4), and (5), where cov(**X**, **Y**) represents the covariance between predicted value (**X**) and ground truth (**Y**), i.e., the simulated ignition delay using CHEMKIN PRO, σ_X and σ_Y represent the standard deviation in **X** and **Y**, respectively, x_i and y_i represent the vector of predicted value and ground truth, respectively, and N represents data points number in the testing set:

$$\rho(\mathbf{X}, \mathbf{Y}) = \frac{\mathrm{cov}(\mathbf{X}, \mathbf{Y})}{\sigma_X \sigma_Y}, \tag{3}$$

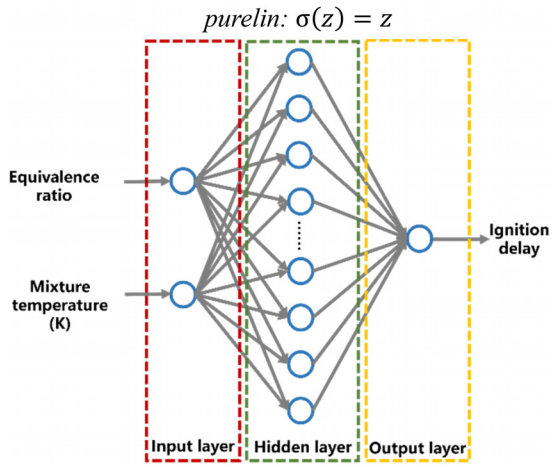

FIG. 5. The BP neural network structure.

$$\mathrm{MSE} = \frac{1}{N}\sum_{i=1}^{N}(x_i - y_i)^2, \tag{4}$$

$$\mathrm{MRE}\,\% = \frac{1}{N}\sum_{i=1}^{N}\left|100 \times \frac{(x_i - y_i)}{y_i}\right|. \tag{5}$$

III. RESULTS AND DISCUSSION

A. Flame characteristics at different overall phi conditions

To investigate the characteristics of flame development progress at different overall phi close to misfire at low load conditions, the overall phi varied, including 0.12, 0.18, and 0.24. The DI pressure and DI timing are selected as 600 bar and −25 °CA ATDC (crank angle after top dead center), respectively. The in-cylinder conditions at different overall phi are illustrated in Fig. 6. It can be found that with the overall phi increasing, the starting point of high temperature heat release (HTHR) advances moderately. The in-cylinder pressure curve peak and HRR curve peak also increase. When the overall phi is 0.12, the HRR curve shows that the weak heat release process exists during −5 to 0 °CA ATDC, indicating that this boundary condition is close to misfire.

At different overall phi conditions, flame natural luminosity images are illustrated in Fig. 7. The number represents the crank angle and light intensity enhancement factor in the upper and lower right corner, respectively. When the overall phi is 0.12 (Fig. 7 upper panel), though it is close to misfire, a few autoignition flame kernels are shown in the combustion chamber at the initial stage of combustion (e.g., before −2.00 °CA). These flame kernels cannot cause spontaneous combustion of its surrounding mixture or sustain flame propagation, thus resulting in misfire. This is featured by the inability to maintain the increase in in-cylinder pressure and HRR, as observed in Fig. 6. With the overall phi increasing, the flame natural luminosity intensity and the number of flame kernels clearly increase. When the overall phi is 0.24 (Fig. 7 lower panel), it is clear that the two initial flame kernels evolve into sustainably propagating flames. In the middle stage of combustion, the flame area (e.g., −3.44 °CA) is considerably greater than that at the overall phi of 0.12 (e.g., −3.08 °CA). This corroborates the trends illustrated in Fig. 6, where greater heat release rate and peak pressure are observed at overall phi of 0.24.

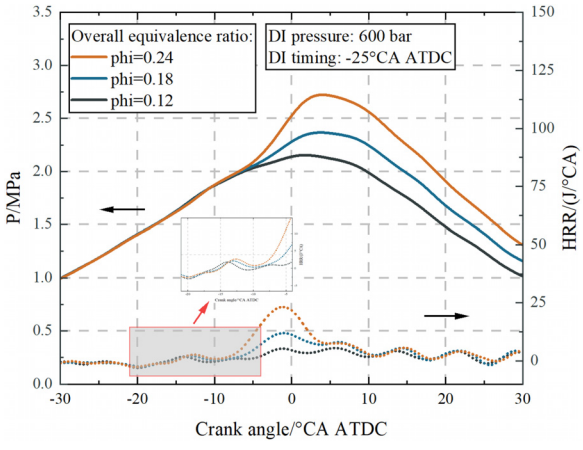

FIG. 6. The in-cylinder conditions at different overall phi. (Solid lines: in-cylinder pressure. Dotted lines: heat release rate.)

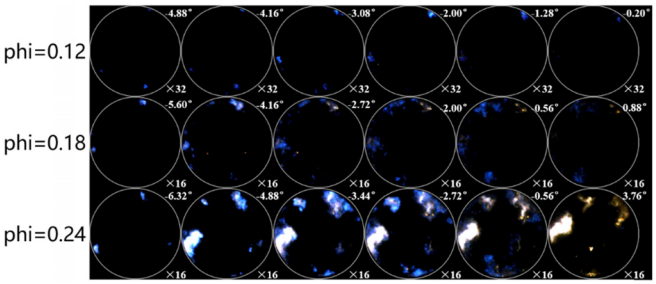

FIG. 7. Flame natural luminosity images at different overall phi.

To better understand the underlying mechanism governing misfire, the fuel-tracer PLIF method is utilized to quantify the in-cylinder local phi. The local phi distribution at different overall phi is illustrated in Fig. 8. Four different timings are selected, namely −20, −15, −10, and −7 °CA. −20 °CA represents a timing close to the injection timing, while −15, −10, and −7 °CA approximately mark the onset of low temperature heat release (LTHR), the end of LTHR, and the start of HTHR, as shown in Fig. 6. It is seen from Fig. 8 that when the fuel spray proceeds to −20 °CA, the local phi of the fuel spray is still maintained at a high level, even though the overall phi is only 0.12. The local phi in the central region of the fuel spray is generally in the range of 3–5, with the densest region exceeding 6. For the conditions of overall phi of 0.18 and 0.24, since it is still in the fuel injection duration at −20 °CA, the local phi exceeds 9 in the densest region. With the fuel spray further developing, the surrounding air is entrained into the fuel spray, and the local phi gradually decreases. At −15 °CA, the fuel spray on the left impinges on the combustion chamber wall, and the fuel spray spreads along the combustion chamber wall arc due to the injection momentum. Compared with the condition of overall phi of 0.12, when the overall phi increases to 0.24, the local phi in the fuel spray on the left of the visualization window increases to around 0.6–1.4 along the injection direction, with the densest region reaching 2. It is worth noting that there is a 40 mm gap on the right side of the visualization area to allow the laser sheet to enter, so the rightmost fuel spray does not impinge on the combustion chamber wall. As for other fuel sprays, the impingement spot is beyond the laser visualization region.

According to the study from Wang *et al.*,[28] the air–fuel mixture recirculation zone is formed in the cambered region of the combustion chamber wall between the two adjacent fuel spray impingement spots. The downstream vortex structures formed by the two adjacent fuel spray impinging on the combustion chamber collide in the recirculation zone and rotate in the opposite directions, thus enhancing turbulent disturbances in the recirculation zone and having an important impact on the formation of initial autoignition flame kernels. The effects of enhancing local phi via recirculation zone is more pronounced at higher overall phi conditions (e.g., 0.18 and 0.24) as illustrated in Fig. 8, as highlighted by the red boxes. It is worth noting that the clockwise vortex exists inside the cylinder. This is most obvious at the overall phi of 0.24, as highlighted in Fig. 8 (cf. red boxed region at −10 °CA). As the crankshaft angle increases, the recirculation zone also moves along the clockwise direction. At −7 °CA where it is close to HTHR, the local phi is significantly lower at the condition of overall

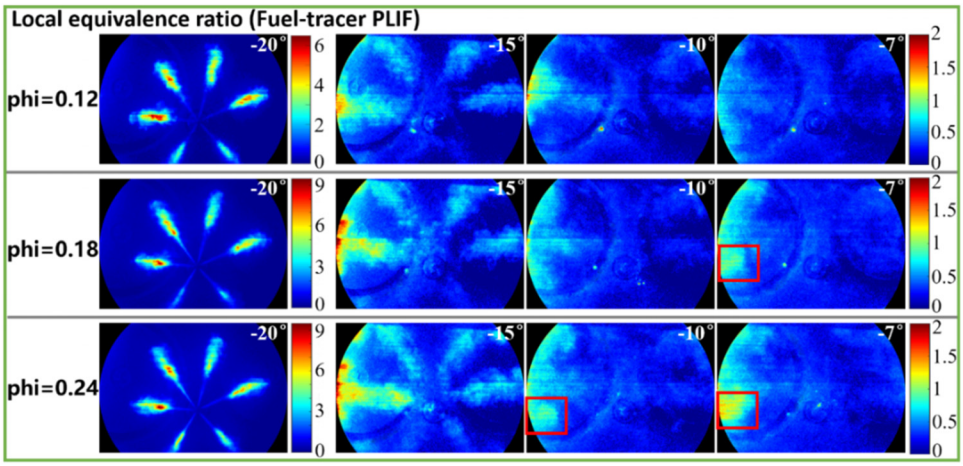

FIG. 8. The local phi distribution at different overall phi.

phi of 0.12 when compared with that at the conditions of overall phi of 0.18 and 0.24.

Formaldehyde has been widely used as the marker of LTHR, and it is usually excited by the 355 nm laser and utilized to indicate the intensity of low temperature chemistry. The OH radical is dominantly produced via H_2O_2 decomposition at intermediate to high temperatures, which can be utilized to represent the intensity of high temperature chemistry. The formaldehyde PLIF images and OH^* natural luminosity images at different overall phi are illustrated in Figs. 9 and 10, respectively. The images in Fig. 9 span from −15 to −6 °CA, to enclose the entire LTHR process as observed in Fig. 6, while the images in Fig. 10 covers the range of −7.5 to −3 °CA, to represent the HTHR regime. Immediately seen from Fig. 9 are the obvious PLIF signals of formaldehyde at −15 °CA under all three phi conditions, indicating that LTHR has already been triggered. At this timing, it is clear that the signal is the strongest under the overall phi of 0.18. This aligns well with the trend observed in Fig. 6, where LTHR onset is the earliest under the overall phi of 0.18. At −11 °CA, the formaldehyde PLIF signal is enhanced at all conditions since this timing approximately corresponds to maximum LTHR, as can be seen from Fig. 6. Particularly, when the overall phi is 0.24, the formaldehyde PLIF signal is enhanced as highlighted by the red box (recirculation zone) in Fig. 9, resulting from better mixing of fuel and air within this region, as can be inferred from Fig. 8 (lower panel) where the local phi at the vortex is around 1.0 at −10 °CA. At −6 °CA, where it is close to the commencement of HTHR, most of the formaldehyde PLIF signal disappears for the overall phi of 0.24. As for the conditions of the overall phi of 0.12 and 0.18, the formaldehyde PLIF signal is still observed at −6 °CA, with a more even distribution observed for the case of 0.12. Again, these trends agree with the HRR results in Fig. 6 where the LTHR duration under the overall phi of 0.24 is the shortest.

Comparing the formaldehyde PLIF images with the OH^* natural luminosity images illustrated in Fig. 10, it is clear that OH radicals are not massively produced until CH_2O is mostly consumed. The OH^*

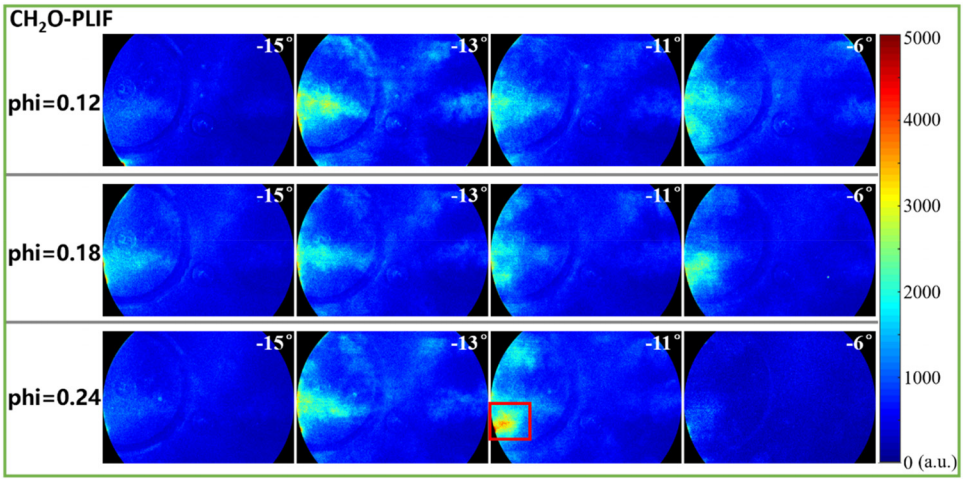

FIG. 9. In-cylinder formaldehyde PLIF signal distribution at different overall phi.

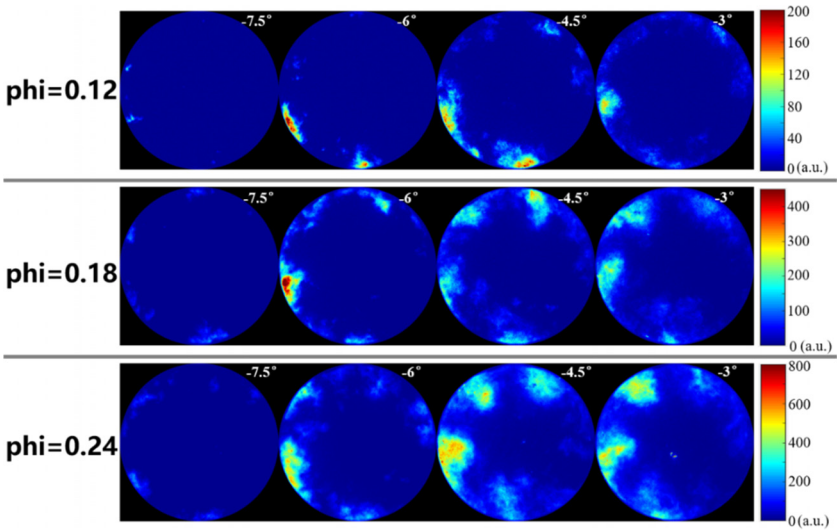

FIG. 10. In-cylinder OH* natural luminosity signal at different overall phi.

signals overlap highly with the initial flame kernels as observed in Fig. 7, indicating that OH radicals are critical to the evolution of flame kernels. Under the overall phi of 0.12 (Fig. 10, upper panel), the OH* signal area and intensity are the lowest among the three conditions. The generated OH radicals quickly dissipate at −3 °CA, as the adjacent mixture is too lean to sustain the production of OH radicals. As a result, the initial flame kernels cannot evolve into a stably propagating flame, hence misfire. As the overall phi increases to 0.24, due to the enhanced local phi near the initial flame kernels via pronounced recirculation (c.f., Fig. 8), the initial flame kernels evolve into flame fronts that propagate stably, as can be inferred from expanding the OH* signal area and the enhanced signal intensity in Fig. 10 (lower panel).

B. Flame development features at close to misfire conditions

To further examine the flame development features under PPC mode at close to misfire conditions, two typical flame development features are illustrated in Fig. 12, including a multipoint autoignition dominated combustion cycle under the HCCI mode and a flame propagation dominated combustion under the RCCI mode at close to misfire conditions. Engine operation conditions under HCCI mode and RCCI mode at close to misfire conditions can be found in Table II.

Under the HCCI mode, the DI timing was −180 °CA to form relatively homogeneous air–fuel mixtures. However, many relevant studies have demonstrated that there is the existence of certain mixture concentration and temperature heterogeneity inside the combustion chamber.[29,30] The combustion process of HCCI is dominated by multipoint autoignition as illustrated in Fig. 12, in which several blue initial flame kernels are generated simultaneously throughout the combustion chamber. The flame kernels develop rapidly and fill the entire combustion chamber in a short time, resulting in high peaks of in-cylinder pressure and heat release rate as illustrated in Fig. 11.

Under the RCCI mode at close to misfire condition, the flame development pattern changes significantly. As illustrated in Fig. 12 (lower panel), the homogeneous low reactivity charge is ignited by the high reactivity charge, and only one autoignition flame kernel is formed. Because the piston is moving downward, the in-cylinder thermodynamic environment decreases, which cannot assist in the formation of new autoignition flame kernels. The single flame kernel develops mainly via low-speed flame propagation, which is similar to that of spark-ignited engine. At 23.56 °CA, other two small initial autoignition flame kernels are formed in the upper part of the combustion chamber, though the number of flame kernels is still limited. Therefore, as illustrated in Fig. 11, the in-cylinder pressure curve and HRR curve show a slight increase far away from TDC. Compared to the two combustion modes, the flame development features of PPC, especially at close to misfire condition, are more complicated. Whether PPC misfire is governed by the characteristics of flame propagation or multipoint autoignition dominated combustion remains unclear.

Flame development features at different combustion modes and operation conditions are illustrated in Fig. 13. The flame area and the number of flame kernels are identified via the Image Region Analyzer Tool in MATLAB with proper thresholds used. The averaged flame area is calculated by the flame area divided by the number of flame kernels. It should be noted that in Fig. 13, the combustion onset

TABLE II. Engine operation conditions under HCCI mode and RCCI mode at close to misfire conditions.

Combustion mode	PI fuel	PI timing (°CA ATDC)	DI fuel	DI timing (°CA ATDC)	$(PI/DI)_{vol}$	Injection masses per cycle (mg/cyc equivalent heat of n-heptane)
HCCI	···	···	N-heptane	−180	0:10	16.6
RCCI	Methanol	−360	N-heptane	−15	7:3	34.0

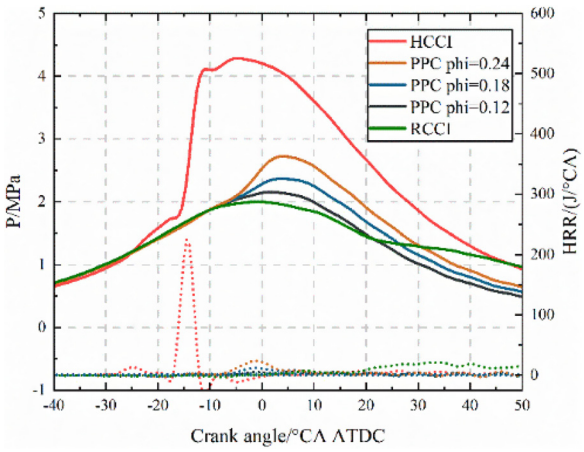

FIG. 11. The in-cylinder conditions at different combustion modes (Solid lines: in-cylinder pressure. Dotted lines: heat release rate).

timing, which is the timing when the light signal in flame natural luminosity images is first recorded, is shifted to the same timing to conveniently compare the flame development features under different combustion modes and operation conditions. The flame area characteristics are selected for analysis as they can be used to identify the flame propagation or multipoint autoignition dominated combustion pattern.

In Fig. 13(a), it can be found that the multipoint autoignition dominated combustion under the HCCI mode features the most rapid speed to reach the maximum flame area, which needs merely 1.80 °CA and corresponds to 0.25 ms at the engine speed of 1200 rpm. On the other hand, the flame propagation dominated combustion under the RCCI mode at close to misfire condition features a very low speed to reach its maximum flame area, which takes 21.96 °CA (3.05 ms) and is about 12 times longer than that of multipoint autoignition dominated combustion. The first derivative of flame area with respect to flame development time can serve as an indication of flame development speed. Similar trends can also be seen from the first derivative of flame area as illustrated in Fig. 13(b), where the peak value under the HCCI mode is significantly higher than that under that RCCI mode. It is obvious in Fig. 13(a) that the flame area under the PPC modes cannot reach those under the HCCI and RCCI modes. This is expected, as under both HCCI mode and RCCI modes, the combustion chamber is charged with a relatively homogeneous mixture that can sustain flame development throughout the combustion changer. However, under the PPC modes where direct fuel injection is used, significant concentration stratification presents in the combustion chamber. With such stratification, flame cannot develop toward the leaner region of the combustion chamber, hence a smaller flame area. With the overall phi decreasing, the flame area under the PPC mode decreases considerably.

The number of flame kernels under different combustion modes is illustrated in Fig. 13(c). Under the HCCI mode, the number of flame kernels displays a rapid increase to 12, leading to a great value in the first derivative of the number of flame kernels as illustrated in Fig. 13(d). After ∼0.72 °CA, the individual flame kernels merge to form a larger flame area, and the number of flame kernels begins to decrease rapidly. A characteristically different trend is observed under the RCCI mode, where the number of flame kernels remains at a low level (e.g., no more than three) throughout the combustion process. The corresponding first derivative of the number of flame kernels shows a very limited rate of flame generation and mergence under this combustion mode. Under the PPC modes, the development pattern of the number of flame kernels is between that under the HCCI mode and that under the RCCI mode. When the overall phi is 0.18 and 0.24, the number of flame kernels has a similar peak with that observed under the HCCI mode, though with a lower increasing rate and stronger oscillations, as can be seen in Fig. 13(d). When the overall phi is 0.12, the number of flame kernels is less, which decreases rapidly as the flame kernels are quenched by the low local phi (cf. Figs. 7 and 8).

The averaged flame area is illustrated in Fig. 13(e). Although the number of flame kernels under the PPC modes (i.e., phi = 0.18 and 0.24) is similar to that under the HCCI mode, the average flame area under the PPC modes is significantly lower, indicating that smaller initial flame kernels are favored under the PPC modes. Without the subsequent flame development for individual flame kernels, the averaged flame area becomes limited. This is most obvious at the overall phi of 0.12, where the averaged flame area is close to zero.

Overall, the multipoint autoignition dominated combustion mode (i.e., the HCCI mode) features rapid and more pronounced development in flame area, the number of flame kernels and averaged flame area, while the flame propagation dominated combustion mode (i.e., the RCCI mode at close to misfire condition) exhibits a prolonged flame development process with the least number of flame kernels. As for the PPC modes, although the number of flame kernels is relatively high at relatively higher overall phi condition, the averaged flame area

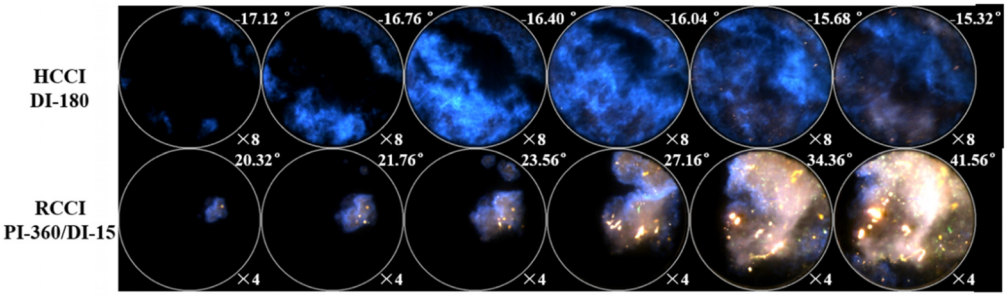

FIG. 12. Two different flame development features including multipoint autoignition dominated combustion for HCCI and flame propagation dominated combustion for RCCI at close to misfire condition.

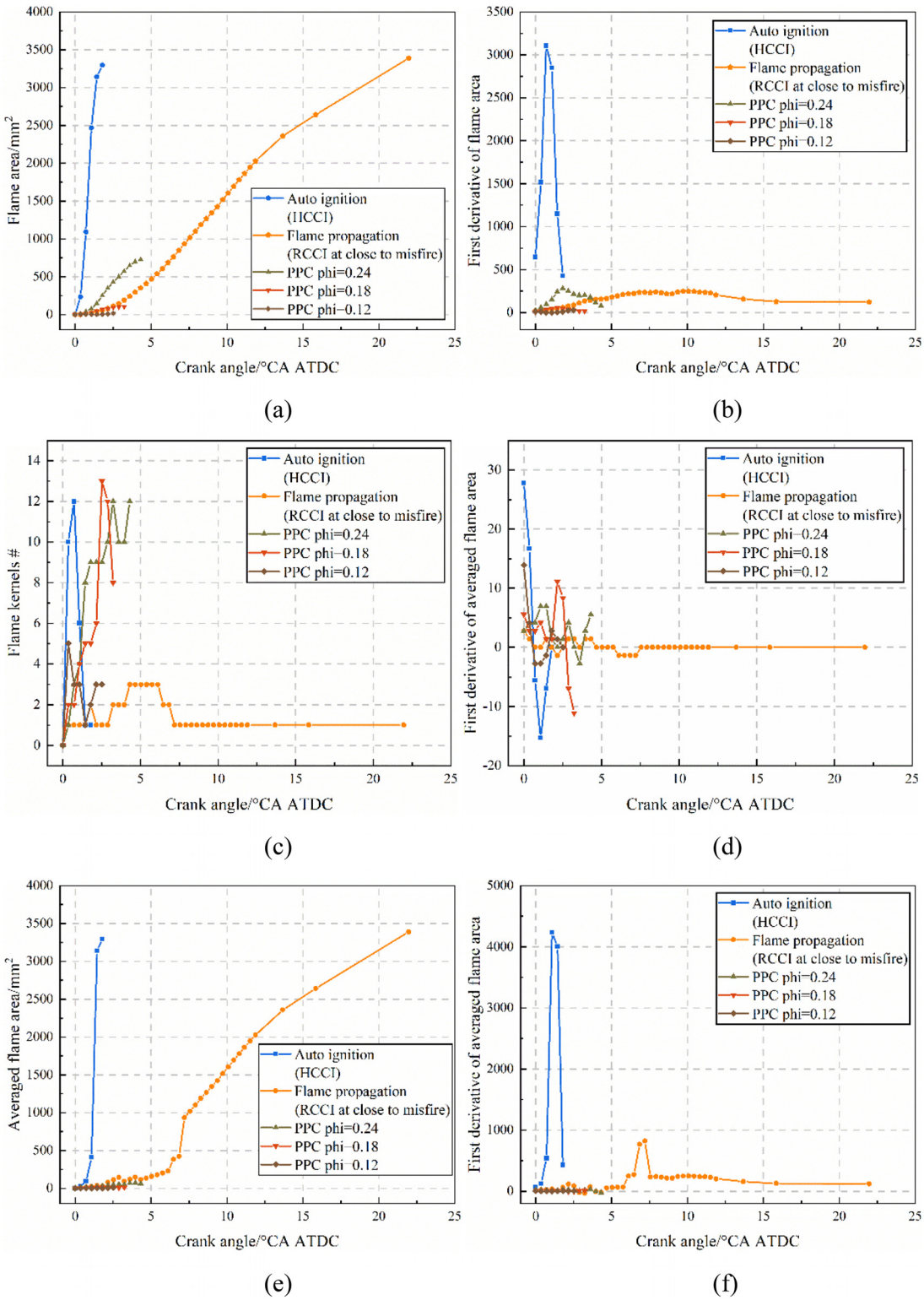

FIG. 13. Flame development features at different combustion modes and operation conditions. (a) Flame area, (b) first derivative of flame area, (c) number of flame kernels, (d) first derivative of the number of flame kernels, (e) averaged flame area, and (f) first derivative of averaged flame area.

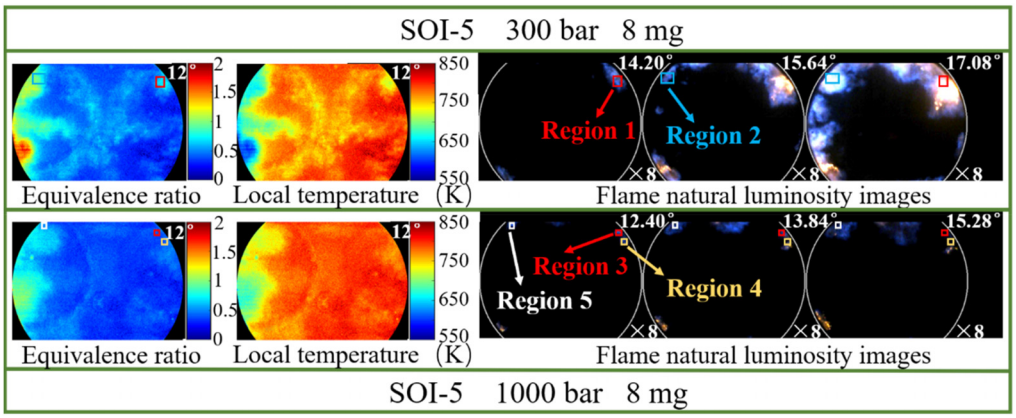

FIG. 14. The local phi and temperature distribution in different regions under the PPC modes.

remains small. At close to misfire condition (e.g., overall phi of 0.12), the number of flame kernels, the averaged flame area, and the maximum flame area are seriously limited.

C. Machine learning-assisted kinetic analyses

With the local phi and temperature distribution, the boundary conditions behind the misfire region can be quantified for further analysis and prediction. The local phi and temperature distribution in different regions are illustrated in Fig. 14. The DI timing was fixed at −5 °CA, and the DI fuel mass per cycle was 8 mg (corresponding to an overall phi of 0.24), while the DI pressure varies from 300 to 1000 bar. A stable combustion is seen at lower DI pressure, while at higher DI pressure, the flame is faint and close to misfire. The reason for this has been well explained in our previous study.[25]

To further investigate the controlling mechanism for stable combustion and misfire in the specific region, five different regions, referred to as Region 1 to Region 5 as marked in Fig. 14, are selected based on their different flame development patterns. Region 1 and Region 2 feature large flame area and strong flame natural luminosity intensity with stable combustion. Region 3 and Region 4 represent regimes close to misfire, where sporadic flame kernels are generated but cannot develop into propagating flames. Region 5 represents a local environment that is in between misfire and stable combustion.

The local phi and local temperature are extracted from each pixel of the five regions in Fig. 14, which are overlayed on the isopleths of ignition delay times in a 2D space covering phi from 0.3 to 1.3 and temperatures from 640 to 820 K, as illustrated in Fig. 15. The ignition delay times are obtained using CHEMKIN PRO, assuming an adiabatic and homogeneous n-heptane/air mixture at a fixed pressure of 18 bar (taken from measured in-cylinder pressure at 12 °CA ATDC). Immediate seen from Fig. 15 is the scattering in local phi and local temperature in all the regions, with a trade-off correlation observed between the two parameters. This correlation is expected as the richer region will experience more fuel evaporation effects, leading to lower local temperatures. It is obvious from Fig. 15 that misfire under the PPC mode is governed by the local phi and local temperature that directly dictate the local autoignition reactivity. Specifically, the leanest local mixtures in Region 1 and Region 2 are easy to autoignite (e.g., close to the purple box that marks the regime with the shortest ignition delay), leading to the formation of initial flame kernels, as observed in Fig. 14. These flame kernels are surrounded by richer mixtures (e.g., with local phi of 0.8–1.1, as can be seen from Fig. 15) that allow the development of stably propagating flames. However, the local mixtures in Region 3 and Region 4 are extremely lean (e.g., local phi < 0.4), with relatively longer ignition delay. As such, flame kernels are less likely to form within these two regions, or quickly quenched by the surrounding lean mixtures if formed, as indicated by the flame natural luminosity images in Fig. 14. Therefore, these regions fall within the misfire regime, as highlighted by the green box in Fig. 15. Region 5 almost overlaps with the purple box, indicating that the local mixtures in Region 5 are the most reactive to form initial flame kernels. Nevertheless, the ensuing fate of the initial flame kernels in this region can differ considerably, leading to either misfire or stable flame propagation depending on the balance in local temperature and local phi.

The ignition delay map in Fig. 15 can be misleading if the chemical kinetic model used is inadequate to represent the autoignition reactivity of the local mixtures at various thermodynamic conditions. In this regard, the model is further validated against the local flame development patterns that are recorded from the experiments. Given the strong link between local autoignition reactivity and flame

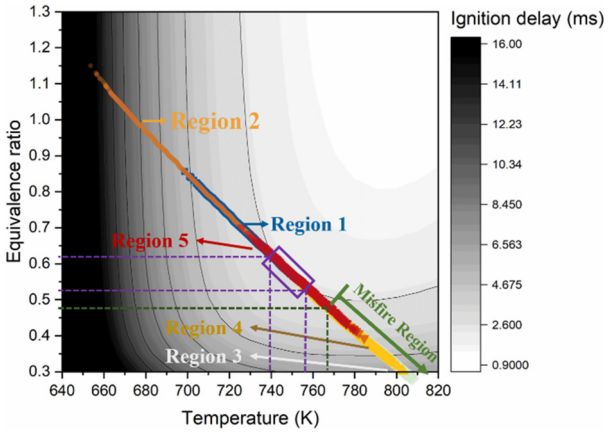

FIG. 15. The ignition delay distribution in different regions at 12 °CA ATDC.

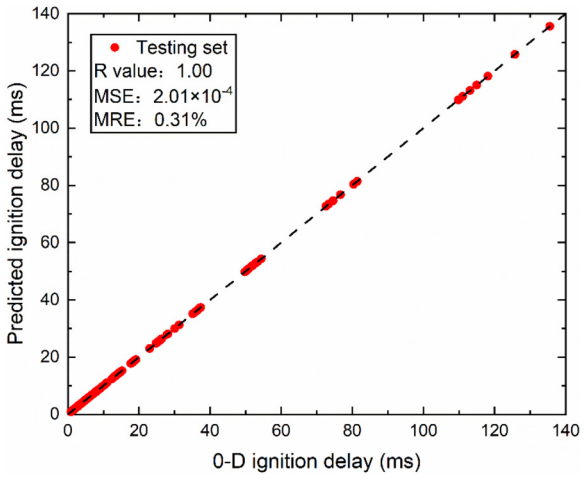

FIG. 16. Comparison between 0-D ignition delay simulated using CHEMKIN-PRO and the predicted ignition delay from the BP neural network.

development characteristics, simulated ignition delay times are used for comparisons. The simulations are conducted in the same way as that used for Fig. 15. In addition, to generate a continuous response of ignition delay time to local thermodynamic conditions, a BP neural network is trained on the discrete simulated ignition delay times, following the procedure outlined in Sec. II E. The BP neural network maps the autoignition reactivity to the two critical parameters as concluded in foregoing discussions, i.e., local temperature and local phi. On the basis of this neural network, a spatially continuous surface of ignition delay can be generated with infinite resolution, based on which in-depth comparison with experiments can be established. The comparisons between the ignition delay simulated using CHEMKIN-PRO and that predicted from BP neural network are illustrated in Fig. 16. The trained BP neural network replicates the original model commendably, with an R value of 1.0, an MSE of 2×10^{-4}, and an MRE of 0.31%.

The ignition delay contours in Region 1 and Region 3 at 12 °CA ATDC mapped by the BP neural network are shown in Fig. 17 along with the respective flame natural luminosity images at a slightly later

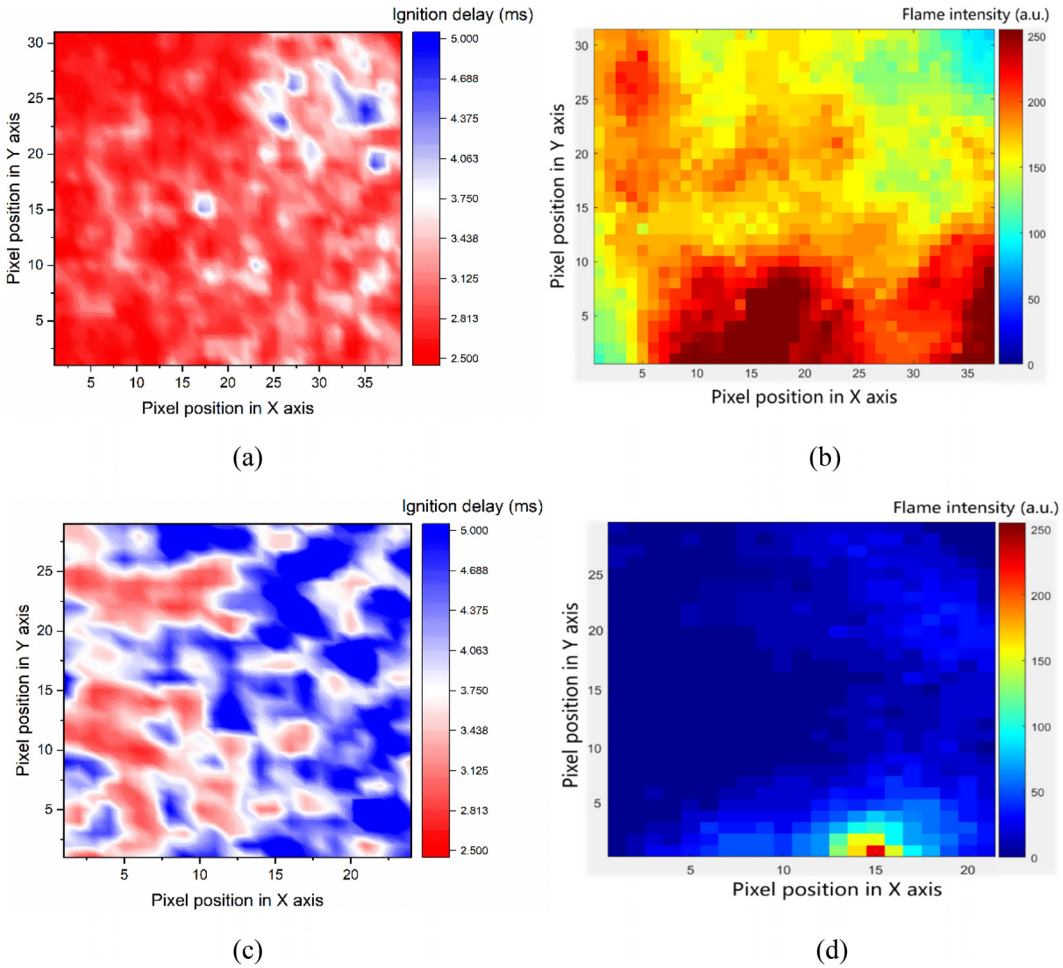

FIG. 17. Ignition delay distribution maps at 12 °CA ATDC predicted by the BP neural network in (a) Region 1 and (c) Region 3, along with the experimental images of flame natural luminosity intensity at 15.28 °CA ATDC in (b) Region 1 and (d) Region 3.

timing (i.e., 15.28 °CA ATDC). First seen from Fig. 17 is the good correspondence between the predicted ignition delay contours and the experimental images. Specifically, in Region 1, most local mixtures have high autoignition reactivity except those located around the top-right corner. As a result, these mixtures quickly autoignite, forming initial flame kernels that subsequently develop into propagating flames. This is supported by the recorded flame intensity distribution, as shown in Fig. 17(b), where the flame develops at the left and bottom areas and propagates to the top-right area where autoignition reactivity is low. On the other hand, as most of the local mixtures in Region 3 [Fig. 17(c)] is highly resistant to autoignition, although ignition kernels can be generated, these ignition kernels are sparsely distributed, as seen in Fig. 17(a), and are subsequently quenched by the unreactive surrounding mixtures. Consequently, the mixture within this region misfires, as corroborated by the experiments illustrated in Fig. 17(d).

It is clear from the foregoing discussions, particularly Figs. 15 and 17, that strong correspondences exist between flame development characteristics and local autoignition reactivity. To further elucidate the chemical kinetic cause for the different flame development patterns observed in Fig. 14, heat rate of production for individual reaction is analyzed at three representative conditions, namely phi = 1.0 and T = 674 K, phi = 0.58 and T = 747 K, and phi = 0.30 and 803. These three conditions represent Region 1, Region 5, and Region 3, respectively, which are extracted from the pixels in the flame luminosity images, and are referred to as conditions 1, 2, and 3, respectively, in the following. The analysis is performed at maximum preliminary heat release rate before HTHR, which corresponds to 9.22, 2.58, and 6.00 ms for conditions 1, 2, and 3, respectively, as illustrated in Fig. 18(a). The results for the top ten exothermic reactions are summarized in Fig. 18(b), along with the calculated heat release rate displayed in Fig. 18(a).

It can be seen from Fig. 18(b) that preliminary heat release at all conditions are dominated by CH_2O chemistry, with $HCO + O_2 = CO + HO_2$ being the top contributor and $CH_2O + OH = HCO + H_2O$ being the second or third contributor (note that $HCO + O_2 = CO + HO_2$ is a reaction specific to CH_2O, as the consumption of CH_2O via H-atom abstraction directly leads to the production of HCO). The direct link between CH_2O consumption and preliminary heat release supports the experimental observations from Fig. 9, where CH_2O is used as an indication to represent preliminary heat release that is critical to initial flame kernel development. As can be seen from Fig. 18, at condition 2, preliminary heat release is intense and fuel autoignition reactivity is high, though the mixture is lean. Therefore, the mixture in Region 1 supports both ignition kernel generation and subsequent flame development. As the condition shifts to condition 1, although the heat release is considerably magnified due to the increase in specific energy density (i.e., more fuel in the mixture at condition 2), the lower local temperature at this condition prolongs the ignition delay. During this delay period, the heat produced from an adjacent ignition kernel can dissipate to the surrounding mixtures, leading to either quenched ignition kernel or propagating flame depending on the competition between local heat production and heat loss. As such, Region 5 is a transition region between misfire and sustainable flame propagation, as shown in Fig. 15. When the mixture becomes even leaner at condition 3, the heat production rate diminishes considerably. Although there is an increase in temperature, the mixture enters the negative temperature coefficient (NTC) region where mixture autoignition reactivity decreases with increasing temperature. As a combination of these effects, both ignition kernels and flame propagation cannot be sustained, hence misfire in Region 3.

IV. CONCLUSIONS

This work investigates the preliminary heat release, autoignition, and flame development characteristics at ultra-lean conditions in a well-controlled optical engine under various combustion modes, via a case study of n-heptane, to comprehend the underlying mechanisms governing misfire at advanced engine conditions that are representative of low-load operations and lean blow-out limits. Comprehensive analyses of experimental and modeling results indicate the following:

- Flame natural luminosity imaging results reveal the characteristically different flame development patterns under the PPC mode, with the corresponding combustion behavior spanning from misfire to stable combustion at overall phi from 0.12 to 0.24, respectively. Further analyses coupling heat release calculation and PLIF/OH* luminosity imaging highlight the strong connections between preliminary heat release and CH_2O production, as well as between flame stability and OH production.

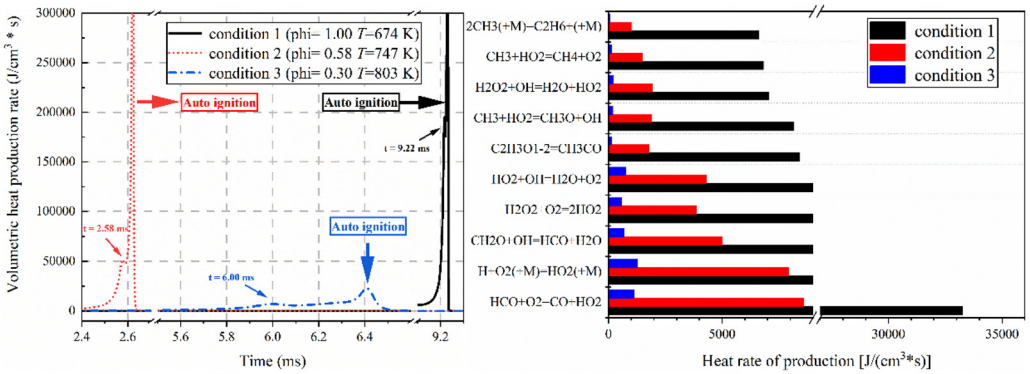

FIG. 18. Analysis of heat rate of production per reaction under different conditions. (a) Volumetric heat production rate vs time. (b) Heat rate of production for top ten reactions.

- The features of flame development, including total flame area, number of initial flame kernels and flame area per kernel at close to misfire condition is further characterized through imaging post-processing. Comparison across the HCCI, RCCI, and three PPC modes indicate two distinctive regimes where the HCCI and RCCI modes display multi-point autoignition and flame propagation dominated combustion, respectively, with the PPC modes falling in between the two regimes, in which initial flame kernels first form via localized autoignition events, then evolve into flame propagation.
- The initial flame kernel generation and the subsequent flame propagation are dictated by the spatial distribution of local phi and local temperature in the mixture, which govern the localized preliminary heat release behavior and autoignition reactivity.
- The chemical kinetic model, in conjunction with the BP neural network, well captures the different regions of flame development, including the stable flame propagation region, the misfire region, and the transition region, via ignition delay time maps with respect to the local phi and local temperature.
- Further kinetic analysis and heat rate of production per reaction analysis highlight the important chemical kinetics that govern the initial flame development patterns, with reactions directly consuming CH_2O (primarily via $CH_2O + OH = HCO + H_2O$ and $HCO + O_2 = CO + HO_2$) as the top contributors to the preliminary heat release that greatly promotes the generation and evolvement of initial flame kernels.

Comprehensive characterizations of preliminary heat release and autoignition behaviors, and their roles in flame initiation and development under various advanced engine operation conditions, including HCCI, RCCI, and PPC modes, are achieved via experimental investigations (e.g., flame luminosity, OH^* luminosity, and CH2O PLIF imaging), theoretical analyses (e.g., characterization of local equivalence ratio, local temperature, initial flame kernel number, and flame area), and ML-informed chemical kinetic analyses (e.g., autoignition mapping via a BP neural network, chemical kinetic modeling with a detailed chemistry model). The obtained data are expansive, which greatly enriches the existing database. Furthermore, the findings herein fill the gap in the community toward understanding, from fundamental perspectives, the flame initiation and development at ultra-lean conditions in advanced combustion concepts, providing valuable insights to guide future operations at low-load conditions and close to lean blow-out limits.

ACKNOWLEDGMENTS

The authors would like to acknowledge the financial support provided by the National Natural Science Foundation of China through the Projects of 51976134 and 51921004. In addition, the authors would also like to acknowledge the support from the Hong Kong Special Administrative Region of China under Grant Nos. P0039589 and P0050998.

AUTHOR DECLARATIONS

Conflict of Interest

The authors have no conflicts to disclose.

Author Contributions

Yanqing Cui: Conceptualization (equal); Data curation (equal); Formal analysis (equal); Investigation (equal); Methodology (equal); Software (equal); Visualization (equal); Writing—original draft (equal); Writing—review & editing. **Haifeng Liu**: Investigation (equal); Resources (equal); Supervision. **Mingsheng Wen**: Software (equal); Validation. **Zhengyang Ming**: Software (equal); Validation. **Zunqing Zheng**: Funding acquisition (equal); Validation. **Yu Han**: Validation. **Song Cheng**: Funding acquisition (equal); Software (equal); Writing—review & editing. **Mingfa Yao**: Funding acquisition (equal); Supervision (equal).

DATA AVAILABILITY

The data that support the findings of this study are available within the article.

REFERENCES

[1]Y. Huang and V. Yang, "Dynamics and stability of lean-premixed swirl-stabilized combustion," Prog. Energy Combust. Sci. **35**, 293 (2009).
[2]V. Raman, Q. L. Tang, Y. Z. An, H. Shi, P. Sharma, G. Magnotti, J. Chang, and B. Johansson, "Impact of spray-wall interaction on the in-cylinder spatial unburned hydrocarbon distribution of a gasoline partially premixed combustion engine," Combust. Flame **215**, 157 (2020).
[3]S. L. Wang, X. D. Zhu, L. M. T. Somers, and L. P. H. de Goey, "Effects of exhaust gas recirculation at various loads on diesel engine performance and exhaust particle size distribution using four blends with a research octane number of 70 and diesel," Energy Convers. Manage. **149**, 918 (2017).
[4]M. Stohr, R. Sadanandan, and W. Meier, "Experimental study of unsteady flame structures of an oscillating swirl flame in a gas turbine model combustor," Proc. Combust. Inst. **32**, 2925 (2009).
[5]J. M. Lourier, M. Stohr, B. Noll, S. Werner, and A. Fiolitakis, "Scale Adaptive Simulation of a thermoacoustic instability in a partially premixed lean swirl combustor," Combust. Flame **183**, 343 (2017).
[6]Z. X. Chen, N. Swaminathan, M. Stohr, and W. Meier, "Interaction between self-excited oscillations and fuel-air mixing in a dual swirl combustor," Proc. Combust. Inst. **37**, 2325 (2019).
[7]Z. G. Zhang, D. Guan, Y. Q. Zheng, and G. N. Li, "Characterizing premixed laminar flame-acoustics nonlinear interaction," Energy Convers. Manage. **98**, 331 (2015).
[8]Y. Z. An, V. Raman, Q. L. Tang, H. Shi, J. Sim, J. Chang, G. Magnotti, and B. Johansson, "Combustion stability study of partially premixed combustion with low-octane fuel at low engine load conditions," Appl. Energy **235**, 56 (2019).
[9]Q. L. Tang, H. F. Liu, M. K. Li, and M. F. Yao, "Optical study of spray-wall impingement impact on early-injection gasoline partially premixed combustion at low engine load," Appl. Energy **185**, 708 (2017).
[10]F. S. Liu, Z. J. Shi, Z. Zhang, Y. K. Li, and C. H. Sun, "Numerical study on critical ambient temperature for auto-ignition of the diesel spray under cold-start conditions," Fuel **258**, 116191 (2019).
[11]Z. J. Shi, F. S. Liu, W. W. Shang, Y. K. Li, C. H. Sun, and M. Zhu, "Numerical study on the influence of injection pressure on the ignition and combustion of *n*-dodecane spray at cold-start conditions," Fuel **264**, 116882 (2020).
[12]H. Y. Chen, Z. J. Shi, F. S. Liu, Y. Wu, and Y. K. Li, "Non-monotonic change of ignition delay with injection pressure under low ambient temperature for the diesel spray combustion," Energy **243**, 123017 (2022).
[13]G. Bansal and H. G. Im, "Autoignition and front propagation in low temperature combustion engine environments," Combust. Flame **158**, 2105 (2011).
[14]C. S. Yoo, Z. Y. Luo, T. F. Lu, H. Kim, and J. H. Chen, "A DNS study of ignition characteristics of a lean iso-octane/air mixture under HCCI and SACI conditions," Proc. Combust. Inst. **34**, 2985 (2013).
[15]M. B. Luong, Z. Y. Luo, T. F. Lu, S. H. Chung, and C. S. Yoo, "Direct numerical simulations of the ignition of lean primary reference fuel/air mixtures with temperature inhomogeneities," Combust. Flame **160**, 2038 (2013).

[16]M. B. Luong, G. H. Yu, T. F. Lu, S. H. Chung, and C. S. Yoo, "Direct numerical simulations of ignition of a lean n-heptane/air mixture with temperature and composition inhomogeneities relevant to HCCI and SCCI combustion," Combust. Flame **162**, 4566 (2015).
[17]L. T. Su, M. Zhang, J. H. Wang, and Z. H. Huang, "Direct numerical simulation of DME auto-ignition with temperature and composition stratification under HCCI engine conditions," Fuel **285**, 119073 (2021).
[18]C. Xu, J. W. Park, C. S. Yoo, J. H. Chen, and T. F. Lu, "Identification of premixed flame propagation modes using chemical explosive mode analysis," Proc. Combust. Inst. **37**, 2407 (2019).
[19]C. Xu, A. Y. Poludnenko, X. Y. Zhao, H. Wang, and T. F. Lu, "Structure of strongly turbulent premixed n-dodecane-air flames: Direct numerical simulations and chemical explosive mode analysis," Combust. Flame **209**, 27 (2019).
[20]K. Aditya, A. Gruber, C. Xu, T. F. Lu, A. Krisman, M. R. Bothien, and J. H. Chen, "Direct numerical simulation of flame stabilization assisted by autoignition in a reheat gas turbine combustor," Proc. Combust. Inst. **37**, 2635 (2019).
[21]O. Schulz, T. Jaravel, T. Poinsot, B. Cuenot, and N. Noiray, "A criterion to distinguish autoignition and propagation applied to a lifted methane-air jet flame," Proc. Combust. Inst. **36**, 1637 (2017).
[22]Y. C. Zhou, C. Zhang, X. Han, and Y. Z. Lin, "Monitoring combustion instabilities of stratified swirl flames by feature extractions of time-averaged flame images using deep learning method," Aerosp. Sci. Technol. **109**, 106443 (2021).
[23]Z. Y. Wang, C. F. Song, and T. Chen, "Deep learning based monitoring of furnace combustion state and measurement of heat release rate," Energy **131**, 106 (2017).
[24]G. E. Karniadakis, I. G. Kevrekidis, L. Lu, P. Perdikaris, S. F. Wang, and L. Yang, "Physics-informed machine learning," Nat. Rev. Phys. **3**, 422 (2021).
[25]Y. Cui, H. Liu, M. Wen, L. Feng, Z. Ming, Z. Zheng, T. Fang, L. Xu, X.-S. Bai, and M. Yao, "Optical diagnostics of misfire in partially premixed combustion under low load conditions," Fuel **329**, 125432 (2022).
[26]M. K. Le, S. Kook, and E. R. Hawkes, "The planar imaging of laser induced fluorescence of fuel and hydroxyl for a wall-interacting jet in a single-cylinder, automotive-size, optically accessible diesel engine," Fuel **140**, 143 (2015).
[27]S. Cheng, C. Saggese, D. Kang, S. S. Goldsborough, S. W. Wagnon, G. Kukkadapu, K. W. Zhang, M. Mehl, and W. J. Pitz, "Autoignition and preliminary heat release of gasoline surrogates and their blends with ethanol at engine-relevant conditions: Experiments and comprehensive kinetic modeling," Combust. Flame **228**, 57 (2021).
[28]Z. K. Wang, P. Stamatoglou, M. Lundgren, L. Luise, B. M. Vaglieco, A. Andersson, M. Alden, O. Andersson, and M. Richter, "Simultaneous 36 kHz PLIF/chemiluminescence imaging of fuel, CH_2O and combustion in a PPC engine," Proc. Combust. Inst. **37**, 4751 (2019).
[29]Z. Q. Zheng, X. H. Fang, H. F. Liu, C. Geng, Z. Yang, L. Feng, Y. Wang, and M. F. Yao, "Study on the flame development patterns and flame speeds from homogeneous charge to stratified charge by fueling n-heptane in an optical engine," Combust. Flame **199**, 213 (2019).
[30]X. B. Duan, M. C. Lai, M. Jansons, G. M. Guo, and J. P. Liu, "A review of controlling strategies of the ignition timing and combustion phase in homogeneous charge compression ignition (HCCI) engine," Fuel **285**, 119142 (2021).